



Li Distribution, Kinematics, and Detailed Abundance Analysis among Very Metal-poor Stars in the Galactic Halo from the HESP-GOMPA Survey

Avrajit Bandyopadhyay¹ , Thirupathi Sivarani² , Timothy C. Beers³ , A. Susmitha², Prasanta K. Nayak⁴ , and Jeewan C. Pandey¹

¹ Aryabhata Research Institute of Observational Sciences, Nainital 263001, India; avrajit.india@gmail.com, avrajit@aries.res.in

² Indian Institute of Astrophysics, Bangalore, India

³ Department of Physics and Astronomy and JINA Center for the Evolution of the Elements, University of Notre Dame, Notre Dame, IN 46556 USA

⁴ Tata Institute of Fundamental Research, Colaba, Mumbai, 400005, India

Received 2021 August 11; revised 2022 August 10; accepted 2022 August 11; published 2022 September 27

Abstract

We present a study on the detailed elemental abundances of newly identified, bright, very metal-poor stars with the detection of lithium, initially observed as part of the SDSS/MARVELS pre-survey. These stars were selected for high-resolution spectroscopic follow-up as part of the HESP-GOMPA survey. In this work, we discuss the Li abundances detected for several stars in the survey, which include main-sequence stars, subgiants, and red giants. Different classes of stars are found to exhibit very similar distributions of Li, which points toward a common origin. We derive a scaling relation for the depletion of Li as a function of temperature for giants and main-sequence stars; the majority of the samples from the literature were found to fall within 1σ (0.19 and 0.12 dex K^{-1} for giants and dwarfs, respectively) of this relationship. We also report the existence of a slope of the Li abundance as a function of distance from the Galactic plane, indicating mixed stellar populations. Most Li-rich stars are found to be in or close to the Galactic plane. Along with Li, we have derived detailed abundances for C, odd-Z, α -, Fe-peak, and neutron-capture elements for each star. We have also used astrometric parameters from Gaia-EDR3 to complement our study, and derived kinematics to differentiate between the motions of the stars—those formed in situ and those accreted. The stellar population of the Spite plateau, including additional stars from the literature, is found to have significant contributions from stars formed in situ and through accretion. The orbits for the program stars have also been derived and studied for a period of 5 Gyr backwards in time.

Unified Astronomy Thesaurus concepts: [Stellar atmospheres \(1584\)](#); [Abundance ratios \(11\)](#); [Stellar abundances \(1577\)](#); [Lithium stars \(927\)](#); [Metallicity \(1031\)](#); [Population II stars \(1284\)](#); [Chemically peculiar stars \(226\)](#); [High resolution spectroscopy \(2096\)](#); [Stellar nucleosynthesis \(1616\)](#); [Nucleosynthesis \(1131\)](#); [Stellar populations \(1622\)](#)

1. Introduction

The discovery of large numbers of very metal-poor (VMP; $[Fe/H] < -2.0$) stars has provided great opportunities to study the pristine conditions that existed in the early universe when these old stellar objects were formed (Beers & Christlieb 2005; Spite et al. 2005; Frebel & Norris 2015; Frebel 2018). Among the many studies that could be conducted with these stars, the detection and measurement of lithium are of particular importance. Lithium is the only element in the periodic table, apart from H and He, that owes its origin (at least in part) to Big Bang nucleosynthesis. All other elements can be produced in stellar interiors or other exotic stellar events.

Lithium is also a very fragile element and is easily destroyed when exposed to higher temperatures, which can be inferred from the observed depletion of stellar Li content as a star ascends the giant branch and the stellar atmosphere is mixed with Li-depleted matter from the stellar interior, due to the convective channels that are opened during this phase. This so-called evolutionary mixing largely depletes lithium, lowering its observed absolute abundance, $A(Li)$.

The pioneering study of Spite & Spite (1982) reported the abundance of Li for a sample of the unevolved, older population of stars in the halo and disk of the Milky Way. A

constant abundance of Li, $A(Li) = 2.2$, was obtained, and subsequently referred to as the “Spite Li plateau.” Over time, it came to be recognized that this level was substantially lower than the cosmological prediction of $A(Li) = 2.7$, based on the baryon density determined by the cosmic microwave background measurements of the Wilkinson Microwave Anisotropy Probe (Spergel et al. 2003; Coc et al. 2004). This discrepancy demonstrates the existence of physical processes that have resulted in the depletion of Li in metal-poor main-sequence turnoff (MSTO) stars. Since then, there have been many studies and efforts to understand the Li plateau and solve the Li problem (e.g., Pinsonneault et al. 1999; Ryan et al. 2002; Korn et al. 2006; Piau et al. 2006; Bonifacio et al. 2007, among many others). A small, but statistically significant slope of the Li plateau was discovered by Ryan et al. (1999) as more stars with Li detection were studied. The decreasing trend of Li abundances with a decrease in metallicity was confirmed by Bonifacio et al. (2007) and Sbordone et al. (2010). Extremely metal-poor (EMP; $[Fe/H] < -3.0$) stars were also found to have Li abundances lower than the Spite plateau (e.g., Bonifacio et al. 2015, and references therein), causing the “breakdown” (Aoki et al. 2009) or “meltdown” of the Spite plateau (Sbordone et al. 2010).

Apart from Li, the abundances of other important elements among VMP and EMP stars are of considerable interest for constraining the pollution of their natal gas clouds by previous stellar generations. They also provide valuable constraints for improvements in models of stellar nucleosynthesis. Additional

Table 1
Observational Details for the Program Stars

Star Name	Object	R.A. J(2000)	Decl. J(2000)	Exp. (s)	S/N	V mag.	$\dot{R}V$ (km s^{-1})
SDSS J002400.64+320311.4	SDSS J0024+3203	00 24 00.64	32 03 11.40	7200	70.3	11.58	−434.0
SDSS J031522.0+212324.6	SDSS J0315+2123	03 15 22.00	21 23 24.60	7200	55.4	11.35	−49.0
SDSS J064301.86+593430.9	SDSS J0643+5934	06 43 01.86	59 34 30.90	8100	71.6	11.44	52.2
SDSS J064655.60+411620.5	SDSS J0646+4116	06 46 55.60	41 16 20.50	9600	43.1	11.14	−285.0
SDSS J065252.76+410506.0	SDSS J0652+4105	06 52 52.76	41 05 06.00	8100	68.0	11.36	98.5
SDSS J102411.84+415146.7	SDSS J1024+4151	10 24 11.84	41 51 46.70	7200	49.5	11.83	194.0
SDSS J114658.70+234357.2	SDSS J1146+2343	11 46 58.70	23 43 57.20	8100	49.1	11.06	−9.5
SDSS J134144.60+474128.9	SDSS J1341+4741	13 41 44.60	47 41 28.90	7200	47.0	12.38	−190.5
SDSS J172548.56+420241.9	SDSS J1725+4202	17 25 48.56	42 02 41.90	8100	53.0	11.66	−266.5
SDSS J193344.73+452410.9	SDSS J1933+4524	19 33 44.73	45 24 10.90	8100	65.5	11.48	157.0
SDSS J193712.01+502455.5	SDSS J1937+5024	19 37 12.01	50 24 55.50	7200	130.0	10.44	−184.0
SDSS J195344.22+422249.9	SDSS J1953+4222	19 53 44.22	42 22 49.90	7200	245.0	9.23	−308.1

discoveries of, in particular, bright stars with $[\text{Fe}/\text{H}] < -2.0$, with or without chemical anomalies, are crucial for a better understanding of the nature of nucleosynthetic events in the early universe.

In this paper, we report Li abundances for 12 metal-poor stars (including 10 VMP stars and one EMP star), nine of which are studied for the first time. We have included three stars with measured Li reported earlier, and use them for investigations of their kinematics. The kinematics of these three stars were not reported previously and are included here for the sake of completeness of this chemodynamical study of Li abundances in stars from the HESP-GOMPA survey. In Section 2, we describe the target selection and details of the high-resolution spectroscopic observations. Derivations of stellar parameters and the measurement of Li abundances are described in Section 3. Implications of these measurements, possible correlations with atmospheric parameters and other abundances, and the kinematics of our sample, supplemented by literature studies, are described in Section 4. Section 5 presents a brief summary and conclusions.

2. Observations, Target Selection, and Analysis

High-resolution ($R \sim 30,000$ and $60,000$) spectroscopic observations of our program stars were carried out as a part of the HESP-GOMPA (Hanle Echelle SPectrograph—Galactic Survey of Metal-poor Stars) survey, using the HESP (Sriram et al. 2018) on the 2 m Himalayan Chandra Telescope at the Indian Astronomical Observatory (IAO). The targets were selected from the spectroscopic pre-survey for MARVELS (Ge et al. 2015), which was carried out as a part of SDSS-III (Eisenstein et al. 2011). This offers the chance to identify bright metal-poor halo stars that could be studied at high spectral resolution using moderate-aperture telescopes. We have used synthetic spectral fitting of the pre-survey data to identify the most metal-poor stars. Furthermore, the metal-poor candidates with weak CH G -bands were given preference for the high-resolution follow-up observations to remove the carbon-rich stellar populations. We have obtained high-resolution data for 60 metal-poor stars, out of which Li could be measured for the 12 program stars listed in Table 1. In this paper, there are nine new stars with measured Li abundances, but the abundance table has not been included for SDSS J195344.22+422249.9. This object is a CEMP-no star, and will be discussed in an upcoming paper on CEMP stars (A. Bandyopadhyay et al., in preparation). Abundances for the remaining eight stars are

discussed below. Complete details for the others, including all of the observed stars in the HESP-GOMPA survey, will be discussed in a separate paper (A. Bandyopadhyay et al., in preparation). The stars were observed at a spectral resolving power of $R \sim 30,000$, spanning a wavelength range of 380–1000 nm. The coordinates and observation details, including duration of observation, signal-to-noise ratio (S/N), V magnitude, and radial velocity (RV) for the program stars are listed in Table 1.

Data reduction was carried out using the IRAF echelle package, along with the publicly available data reduction pipeline for HESP,⁵ developed by Arun Surya. A cross-correlation analysis with a synthetic template spectrum was carried out to obtain the RV for each star. The calculated RVs are listed in Table 1.

We have employed one-dimensional LTE stellar atmospheric models (ATLAS9; Castelli & Kurucz 2004) and the spectral synthesis code TURBOSPECTRUM (Alvarez & Plez 1998) for determining the abundances of the individual elements present in each spectrum. We have considered the equivalent widths of the absorption lines present in the spectra that are less than 120 mÅ, as they are on the linear part of the curve of growth. Version 12 of the TURBOSPECTRUM code for spectrum synthesis and abundance estimates was used for the analysis. The Kurucz database⁶ was used for the compilation of the linelist. We have adopted the hyperfine splitting provided by McWilliam (1998), along with solar isotopic ratios.

The stellar atmospheric parameters of the program stars were derived iteratively. The first estimates for effective temperature were made using photometric colors, $V - K$. Gaia and spectral energy distribution (Bayo et al. 2008) were also used to derive the values of T_{eff} and $\log g$. A grid for stellar models was prepared for a wide range of T_{eff} , $\log g$, and $[\text{Fe}/\text{H}]$. The abundances of the clean Fe I and Fe II lines were measured for each spectrum by the method of equivalent-width analysis. The best fit was determined so that Fe I abundances do not vary with excitation potential, and similar abundances are obtained from Fe I and Fe II lines. The temperatures were then estimated using the wings of $\text{H}\alpha$ lines, which are sensitive to small variations in temperature. We have measured the FWHM of telluric and ThAr lines to broaden the synthetic spectra using the Gaussian profile for the resolution ($R = 30,000$) of HESP.

⁵ <https://www.iiap.res.in/hesp/>

⁶ <http://kurucz.harvard.edu/linelists.html>

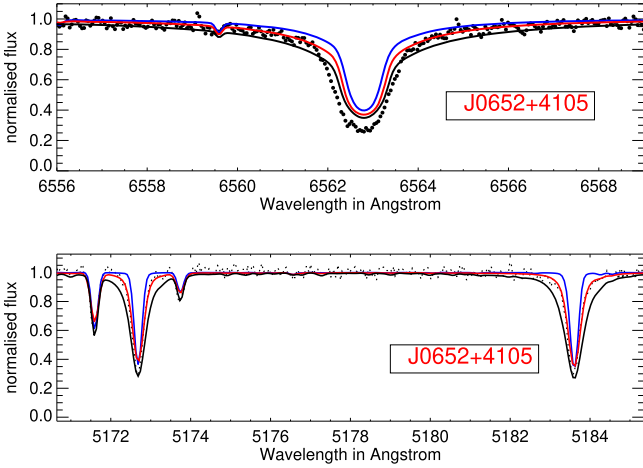


Figure 1. The determination of stellar parameters. The $H\alpha$ feature is shown in the top panel and the wavelength range shown here for the fitting is 6556–6570 Å, while the Mg triplet region is shown in the bottom panel for the wavelength range 5170–5186 Å. In the top panel, the red line indicates the best fit to the wings, while black-filled dots indicate the observed spectrum. A wavelength range of 10 Å on either side of the core is used for fitting the line wing profile. The black and blue lines indicate deviations from the adopted temperature by 150 K. In the bottom panel, the red line denotes the best fit, while the black and blue lines show the deviation from the adopted $\log g$ by 0.50 dex.

The $\log g$ estimated from the Fe I/Fe II lines was assumed for the calculation of the line profile for the Balmer line analysis. The corrections for the non-LTE effects in the estimations of effective temperature from Balmer lines were also incorporated in the adopted values. The color temperatures for the stars were also derived to check for consistency. The different estimates of T_{eff} are listed in Table 2. Similarly, $\log g$ is determined by spectral fitting of the wings of the Mg I triplet in the 5173 Å region. Examples of the fitting for the $H\alpha$ and Mg wings are shown in Figure 1. Independent estimates of $\log g$ were made by other methods as listed in Table 3: (i) ionization equilibrium method using Fe I and Fe II abundances; (ii) using the parallax from Gaia as described below. Surface gravity $\log g$ is calculated using the relation

$$\log(g/g_{\odot}) = \log(M/M_{\odot}) + 4 \log(T_{\text{eff}}/T_{\text{eff}\odot}) + 0.4(M_{\text{bol}} - M_{\text{bol}\odot})$$

The V magnitudes have been taken from SIMBAD and the parallaxes are taken from Gaia⁷ whenever possible. We have used the evolutionary tracks⁸ to estimate the mass of the stars, which is found to be close to $0.8 M_{\odot}$ for metal-poor stars. The finally adopted stellar parameters are listed in Table 4, where we have taken the estimations of $\log g$ using Mg wings due to their sensitivity to small changes in $\log g$ and T_{eff} using Fe I lines because large number of clean Fe I lines could be measured for every star. The parameters were consistent within the typical uncertainties of ~ 150 K for temperature and 0.25 dex for $\log g$. However, we also report a discrepancy between the color temperatures and spectroscopic temperatures for the three stars SDSS J1341+4741, SDSS J1725+4202, and SDSS J1933+4524 as shown in Table 2.

Errors in the derived abundances primarily depend on the S/N of the observed spectra and deviations in the values of the

Table 2
Estimates of Effective Temperature (K) for the Program Stars

Object	$H\alpha$	Fe I	$V - K$	$J - H$	$J - K$
SDSS J0024+3203	5700	5700	5737	5672	5875
SDSS J0315+2123	5450	5400	5570	5287	5264
SDSS J0643+5934	4800	4900	4618	4843	4801
SDSS J0646+4116	5100	5150	5065	5179	5144
SDSS J0652+4105	4900	5000	5060	5108	5060
SDSS J1024+4151	4800	4800	4655	4782	4823
SDSS J1146+2343	5200	5100	5825	5273	5365
SDSS J1341+4741	5450	5450	5927	5438	5749
SDSS J1725+4202	5300	5400	6274	5803	6012
SDSS J1933+4524	5850	5800	6249	6038	6249
SDSS J1937+5024	4950	4800	4738	4702	4908
SDSS J1953+4222	5900	6000	6136	5847	5874

Table 3
Different Estimates of $\log g$ for the Program Stars

Object	Fe I/Fe II	Mg Wings	Gaia Parallax
SDSS J0024+3203	3.80	3.75	3.94
SDSS J0315+2123	4.50	4.50	4.27
SDSS J0643+5934	2.25	2.50	2.28
SDSS J0646+4116	2.25	2.25	2.46
SDSS J0652+4105	2.75	2.50	2.49
SDSS J1024+4151	2.50	2.50	2.38
SDSS J1146+2343	3.10	3.00	3.12
SDSS J1341+4741	2.60	2.50	2.97
SDSS J1725+4202	3.75	3.50	3.90
SDSS J1933+4524	4.40	4.50	4.32
SDSS J1937+5024	1.50	1.50	1.97
SDSS J1953+4222	3.75	4.00	3.97

Table 4
Adopted Stellar Parameters for the Program Stars

Object	T_{eff} (K)	$\log g$ (cgs)	ξ	[Fe/H]	$A(\text{Li})$
SDSS J0024+3203	5700	3.75	1.50	-2.45	2.00
SDSS J0315+2123	5400	4.50	1.00	-2.30	1.80
SDSS J0643+5934	4900	2.50	1.50	-2.90	0.80
SDSS J0646+4116	5150	2.25	1.50	-1.90	1.00
SDSS J0652+4105	5000	2.50	1.50	-2.56	1.75
SDSS J1024+4151	4800	2.50	1.50	-2.25	1.05
SDSS J1146+2343	5100	3.00	1.00	-2.60	1.15
SDSS J1341+4741	5450	2.50	1.80	-3.20	1.95
SDSS J1725+4202	5400	3.50	1.20	-2.50	1.90
SDSS J1933+4524	5800	4.50	1.80	-1.80	2.25
SDSS J1937+5024	4800	1.50	1.50	-2.20	1.00
SDSS J1953+4222	6000	4.00	1.75	-2.25	2.05

adopted stellar parameters. We have used the relation given by Cayrel de Strobel & Spite (1988) to calculate the uncertainty in the abundances due to the S/N. The typical uncertainties in the derived stellar parameters are taken to be ~ 150 K for temperature and 0.25 dex for $\log g$.

3. Abundances

The results of our abundance analysis for eight of the program stars are provided in Tables 6–13. Here we discuss details of this analysis for various classes of elements.

⁷ <https://gea.esac.esa.int/archive/>

⁸ <http://pleiadi.pd.astro.it/>

Table 5
Kinematics for the Program Stars

Object	X (kpc)	Y (kpc)	Z (kpc)	V_x (km s ⁻¹)	V_y (km s ⁻¹)	V_z (km s ⁻¹)	V_R (km s ⁻¹)	L_z (10 ² kpc km s ⁻¹)	V_ϕ (km s ⁻¹)	L_\perp (10 ² kpc km s ⁻¹)
SDSS J0024+3203	-8.19	0.19	-0.12	292.7	-83.0	152.4	-294.6	6.2	76.0	12.12
SDSS J0315+2123	-8.38	0.09	-0.17	27.2	158.4	35.9	-25.5	-13.3	-158.7	2.98
SDSS J0643+5934	-9.00	0.56	0.56	-96.5	131.8	13.2	104.3	-11.8	-125.8	0.96
SDSS J0646+4116	-9.14	0.09	0.31	216.6	-71.7	-208.3	-217.4	6.3	69.4	18.36
SDSS J0652+4105	-9.21	0.09	0.35	-91.0	224.5	12.6	93.2	-20.6	-223.6	1.15
SDSS J1024+4151	-9.06	0.04	1.46	-278.6	-5.6	56.5	278.5	0.6	7.1	1.05
SDSS J1341+4741	-8.13	0.16	0.40	202.4	-79.2	-49.9	-204.0	6.1	75.1	3.25
SDSS J1725+4202	-8.02	0.17	0.12	-218.0	7.8	-7.1	218.1	-0.2	-3.1	0.84
SDSS J1933+4524	-8.05	0.23	0.05	273.3	340.2	72.6	-263.2	-28.0	-348.1	5.98
SDSS J1937+5024	-7.96	1.12	0.27	157.4	58.6	-81.0	-147.6	-6.4	-80.1	6.10
SDSS J1953+4222	-8.07	0.12	0.02	-121.0	-45.9	33.2	120.3	3.8	47.8	2.65

Table 6
Elemental Abundance Determinations for SDSS J0024+3203

Elements	Species	N_{lines}	$A(X)$	Solar	[X/H]	[X/Fe]	σ
Li	Li I	1	2.00				
C	CH	...	6.00	8.43	-2.43	0.02	synth
Na ^a	Na I	2	4.22	6.21	-1.99	0.46	synth
Mg	Mg I	4	5.64	7.59	-1.95	0.50	synth
Al ^a	Al I	1	3.90	6.43	-2.53	-0.08	synth
Si	Si I	2	5.46	7.51	-2.05	0.40	0.09
Ca	Ca I	8	4.37	6.32	-1.95	0.50	0.06
Sc	Sc II	5	1.03	3.15	-2.12	0.33	0.06
Ti	Ti I	7	3.14	4.93	-1.79	0.66	0.09
	Ti II	6	3.03	4.93	-1.90	0.55	0.05
Cr	Cr I	3	3.21	5.62	-2.41	0.04	0.12
	Cr II	2	3.52	5.62	-2.10	0.35	0.07
Mn	Mn I	4	2.62	5.42	-2.80	-0.35	0.11
Co	Co I	2	2.73	4.93	-2.20	0.25	0.06
Ni	Ni I	3	4.16	6.20	-2.04	0.41	synth
Zn	Zn I	2	2.71	4.56	-1.85	0.60	0.07
Sr	Sr II	2	1.00	2.83	-1.83	0.62	synth
Ba	Ba II	2	0.25	2.25	-2.00	0.45	synth
Eu ^b	Eu II	1	-1.0	0.52	-1.52	0.93	synth

Notes. σ indicates the random error.

^a Values obtained after applying NLTE corrections.

^b Indicates an upper limit.

3.1. Lithium

Lithium abundances were derived from the strong absorption features at 6707.76 Å and 6707.98 Å, using the method of spectrum synthesis. The continuum level for the observed spectra is estimated locally around the Li doublet. The observed spectra were fit iteratively with the synthetic spectra for different values of Li abundance, and the best fit was adopted for each star, keeping the Li abundances as the only free parameter in the synthesis. Examples of the spectral synthesis for Li are shown in Figure 2.

Errors in the abundance analysis of Li primarily originate from uncertainties in estimates of effective temperature. A difference of ~150 K is found to alter the Li abundance by 0.14 dex, on average. For the determination of the abundances of neutral species such as Li I, uncertainties in surface gravity play a minimal role.

3.2. The Light and α -elements

Abundances of carbon could be derived for all of the program stars based on the molecular CH G -band in the 4315 Å

Table 7
Elemental Abundance Determinations for SDSS J0315+2123

Elements	Species	N_{lines}	$A(X)$	Solar	[X/H]	[X/Fe]	σ
Li	Li I	1	1.80				
C	CH	...	6.10	8.43	-2.33	-0.03	synth
Na ^a	Na I	2	3.74	6.21	-2.47	-0.17	synth
Mg	Mg I	4	5.85	7.59	-1.74	0.56	synth
Si	Si I	1	5.77	7.51	-1.74	0.56	synth
Ca	Ca I	8	4.24	6.34	-2.10	0.20	0.08
Sc	Sc II	5	-1.04	3.15	-2.11	0.19	0.04
Ti	Ti I	7	3.11	4.93	-1.82	0.48	0.09
	Ti II	6	2.98	4.93	-1.95	0.35	0.13
Cr	Cr I	3	3.08	5.62	-2.54	-0.22	0.08
	Cr II	2	3.19	5.62	-2.43	-0.13	0.09
Mn	Mn I	4	2.60	5.42	-2.82	-0.52	0.12
Co	Co I	2	2.70	4.93	-2.23	0.07	0.06
Ni	Ni I	3	4.26	6.20	-1.94	0.36	synth
Cu	Cu I	2	2.32	4.19	-1.87	0.43	0.12
Zn	Zn I	2	3.09	4.56	-1.47	0.83	synth
Sr	Sr II	2	0.40	2.83	-2.43	-0.03	synth
Ba	Ba II	2	0.25	2.25	-2.00	-0.30	synth

Note.

^a Values obtained after applying NLTE corrections.

Table 8
Elemental Abundance Determinations for SDSS J0643+5934

Elements	Species	N_{lines}	$A(X)$	Solar	[X/H]	[X/Fe]	σ
Li	Li I	1	0.80				
C	CH	...	5.75	8.43	-2.68	0.22	synth
Na ^a	Na I	2	3.54	6.21	-2.67	0.23	synth
Mg	Mg I	4	5.03	7.59	-2.56	0.34	synth
Al ^a	Al I	1	2.70	6.43	-3.73	-0.83	0.09
Ca	Ca I	8	3.61	6.32	-2.71	0.19	0.06
Sc	Sc II	5	0.47	3.15	-2.68	0.22	0.11
Ti	Ti I	7	2.42	4.93	-2.51	0.39	0.10
	Ti II	6	2.36	4.93	-2.57	0.33	0.07
Cr	Cr I	3	2.54	5.62	-3.08	-0.18	0.08
	Cr II	2	3.02	5.62	-2.60	0.30	0.08
Mn	Mn I	4	1.52	5.42	-3.90	-1.00	0.12
Co	Co I	2	2.32	4.93	-2.61	0.29	0.11
Ni	Ni I	3	3.61	6.20	-2.59	0.31	synth
Zn	Zn I	2	1.86	4.56	-2.70	0.20	0.06
Sr	Sr II	2	0.00	2.83	-2.83	0.07	synth
Ba	Ba II	2	-0.50	2.25	-2.75	0.15	synth

Note.

^a Values obtained after applying NLTE corrections.

Table 9
Elemental Abundance Determinations for SDSS J0652+4105

Elements	Species	N_{lines}	$A(X)$	Solar	[X/H]	[X/Fe]	σ
Li	Li I	1	1.75				synth
C	CH		5.75	8.43	-2.68	-0.13	synth
Na ^a	Na I	2	4.23	6.21	-1.98	0.57	synth
Mg	Mg I	5	5.62	7.59	-1.97	0.58	synth
Al ^a	Al I	1	2.96	6.43	-3.47	-0.92	0.18
Ca	Ca I	11	4.14	6.32	-2.18	0.37	0.08
Sc	Sc II	5	1.00	3.15	-2.15	0.40	0.10
Ti	Ti I	4	2.94	4.93	-1.99	0.56	0.15
	Ti II	13	2.78	4.93	-2.15	0.40	0.11
Cr	Cr I	6	3.24	5.62	-2.38	0.17	0.16
	Cr II	1	3.69	5.62	-1.93	0.62	0.09
Mn	Mn I	5	2.71	5.42	-2.71	-0.16	0.12
Co	Co I	2	2.39	4.93	-2.54	0.01	0.08
Ni	Ni I	4	3.82	6.20	-2.38	0.17	synth
Zn	Zn I	1	2.57	4.56	-1.99	0.56	synth
Sr	Sr II	2	1.00	2.83	-1.83	0.72	synth
Y	Y II	2	0.25	2.21	-1.96	0.59	synth
Zr	Zr II	3	0.75	2.59	-1.84	0.71	synth
Ba	Ba II	2	0.50	2.25	-1.75	0.80	synth
La	La II	2	-0.87	1.11	-1.98	0.57	synth
Nd	Nd II	2	0.0	1.42	-1.42	1.13	synth
Eu	Eu II	1	-1.0	0.52	-1.52	1.03	synth

Note.

^a Values obtained after applying NLTE corrections.

region as shown in Figure 3. Most of the stars have low C, the range varying from $[C/Fe] = -0.53$ to $[C/Fe] = +0.22$. Corrections to the measured carbon abundances due to the evolutionary effects were computed based on Placco et al. (2014) and were found to be minimal (0.0–0.01 dex) for the program stars; they have been incorporated in the final reported C abundances in the tables. The poor S/N in the region of the CN band at 3883 Å did not allow for precise abundances for N, while the O lines at 6300 Å and 6363 Å were too weak and dominated by telluric contamination, which prevented a meaningful derivation of O abundances for most of the stars. Oxygen could be derived for SDSS J102411.84+415146.7 and was found to be enhanced, $[O/Fe] = +1.56$.

Among the odd-Z elements, Na and Al could be detected and measured for all of the program stars. The Na abundances were determined using the D1 and D2 lines at 5890 Å and 5896 Å; the Al abundances were measured based on the resonance line at 3961.5 Å. Non-LTE (NLTE) corrections for both the elements, based on Andrievsky et al. (2007, 2008), were also implemented, as reported in Tables 6–13. The mean abundances are shown in comparison to samples from Cayrel et al. (2004) and Cohen et al. (2004) in Figure 4. In this study, Si abundances could be derived for five stars out of the total sample of 11 stars. The abundances are mostly based on the line at 410.29 nm (and also 390.55 nm in a few stars with high blending from the CH line), which falls in the wings of the H δ line as well as having a very poor signal-to-noise ratio. However, the average Si abundances in our study agree well with Cayrel et al. (2004) as demonstrated in Figure 4, but the Si abundances for Cohen et al. (2004) are lower due to the spectral syntheses to determine the abundance of Si in the C-rich stars. These yield abundances of Si that are substantially lower than those obtained with the standard analysis and are indicated in Tables 4–7 and the lower panel of Figure 4 in Cohen et al. (2004). Similarly, carbon is also higher, primarily due to the

evolutionary effects. The spectral synthesis is known to yield more accurate abundances for the weaker lines and low S/N of the spectra and a mixture of the two methods has been used in this study. The uncertainties in the abundances for each element have also been indicated in Figure 4.

The α -elements are produced in different astrophysical sites, such as the hydrostatic burning phases in the shells of massive stars, oxygen and neon burning in Type II supernovae, and hypernovae. Among the α -elements, Mg, Ca, and Ti abundances could be derived for all of the program stars, but meaningful Si abundances could only be derived for a few stars due to the poor S/N toward the blue end of the spectra. Several lines of Mg, Ca, and Ti could be detected in the spectra; the method of equivalent widths was employed to determine the abundances for the stronger lines, while spectral synthesis was used to determine abundances from the weaker and blended features.

Uncertainties in the derived abundances primarily depend on the S/N of the observed spectrum and deviations in the values of the adopted stellar parameters. We have used the relation given by Cayrel de Strobel & Spite (1988) to calculate the uncertainty in the abundances due to the S/N. Uncertainties due to possible temperature and $\log(g)$ deviations were derived using two different model spectra, the first differing in temperature by ~ 150 K and the second deviating in $\log(g)$ by 0.25 dex. The final values of the abundance errors were obtained by adding the uncertainties arising from all three sources in quadrature. However, the errors in the relative abundance ratios are less sensitive to the errors in the model parameters and depend mainly on the S/N.

3.3. The Fe-peak Elements

The Fe-peak elements (Sc, Fe, Cr, Mn, Co, Ni, and Zn) are synthesized during complete and incomplete Si burning phases in pre-supernovae, as well as during the explosive phase of a Type II supernova. Iron abundances were derived on the basis of several Fe I and Fe II lines; a difference of 0.25 dex was noted, which is in agreement with other analyses of metal-poor stars. The iron abundance of the program stars varies from $[Fe/H] = -1.80$ to -3.20 , with a mean value of $[Fe/H] = -2.40$. The abundances of Cr were measured from Cr I lines, which are known to suffer from strong NLTE effects (Lai et al. 2008; Bonifacio et al. 2009); a mean difference of 0.35 dex was obtained between the Cr I and Cr II lines in the current sample. Manganese abundances were primarily measured using the resonance triplet near 4030 Å, but the poor quality of the spectra in that region led to larger errors. The NLTE corrections for the Mn triplet region increase with decreases in metallicity (Bergemann & Gehren 2008; Bergemann et al. 2019). The mean value for the present sample is $[Mn/Fe] = -0.37$. SDSS J064301.86+593430.9 is very strongly depleted in Mn, with $[Mn/Fe] = -1.00$. Cobalt is a product of complete Si burning, and it tracks the iron content of the star, with the expected scatter due to observational uncertainties. The mean abundance of Co for the present sample is $[Co/Fe] = +0.01$. The nucleosynthesis pattern for the program stars, in comparison to the mean abundances of giant stars from Cayrel et al. (2004) and dwarf stars from Cohen et al. (2004), is shown in Figure 4. As seen in the figure, the derived abundances agree well with the mean abundances from these samples.

Table 10
Elemental Abundance Determinations for SDSS J1024+4151

Elements	Species	N_{lines}	$A(X)$	Solar	[X/H]	[X/Fe]	σ
Li	Li I	1	1.05				
C	CH	...	6.00	8.43	-2.43	-0.18	synth
O	O I	...	8.00	8.69	-00.69	1.56	synth
Na ^a	Na I	2	3.90	6.21	-2.31	-0.06	synth
Mg	Mg I	4	5.76	7.59	-2.03	0.22	synth
Al ^a	Al I	1	2.89	6.43	-3.54	-1.29	synth
Ca	Ca I	8	3.68	6.32	-2.64	0.46	0.09
Si	Si I	2	5.42	7.51	-2.09	0.14	0.16
Sc	Sc II	5	1.08	3.15	-2.23	0.12	0.08
Ti	Ti I	7	3.42	4.93	-1.51	0.74	0.12
	Ti II	6	3.11	4.93	-1.82	0.43	0.09
Cr	Cr I	3	3.25	5.62	-2.37	-0.12	0.13
	Cr II	2	3.50	5.62	-2.12	0.13	0.09
Mn	Mn I	4	2.51	5.42	-2.91	-0.66	0.10
Co	Co I	2	2.46	4.93	-2.47	-0.22	0.06
Ni	Ni I	3	4.22	6.20	-1.98	0.27	synth
Cu	Cu I	1	2.89	4.56	-1.67	0.58	synth
Zn	Zn I	2	2.89	4.56	-1.67	0.58	0.11
Sr	Sr II	2	0.75	2.83	-2.08	0.17	synth
Ba	Ba II	2	0.50	2.25	-1.75	0.50	synth
Eu ^b	Eu II	1	-0.75	0.52	-1.27	0.98	synth

Notes.^a Values obtained after applying NLTE corrections.^b Indicates an upper limit.

Table 11
Elemental Abundance Determinations for SDSS J1146+2343

Elements	Species	N_{lines}	$A(X)$	Solar	[X/H]	[X/Fe]	σ
Li	Li I	1	1.15				
C	CH	...	6.00	8.43	-2.43	-0.17	synth
Na ^a	Na I	2	3.67	6.21	-2.64	-0.04	synth
Mg	Mg I	4	5.39	7.59	-2.00	0.60	synth
Al ^a	Al I	1	2.90	6.43	-3.53	-0.93	synth
Ca	Ca I	8	4.10	6.32	-2.22	0.38	0.06
Sc	Sc II	5	-0.73	3.15	-2.42	0.18	0.01
Ti	Ti I	7	2.83	4.93	-2.10	0.50	0.03
	Ti II	6	2.62	4.93	-2.31	0.29	0.04
Cr	Cr I	3	3.07	5.62	-2.55	0.05	0.05
	Cr II	2	3.49	5.62	-2.13	0.47	0.05
Mn	Mn I	4	2.84	5.42	-2.58	-0.02	0.02
Co	Co I	2	2.36	4.93	-2.57	0.03	0.01
Ni	Ni I	3	4.00	6.20	-2.20	0.40	synth
Zn	Zn I	2	2.57	4.56	-1.99	0.61	0.05
Sr	Sr II	2	0.75	2.83	-2.08	0.52	synth
Ba	Ba II	2	0.25	2.25	-2.00	0.60	synth
Eu ^b	Eu II	1	-1.25	0.52	-1.77	0.83	synth

Notes. σ indicates the random error.^a Values obtained after applying NLTE corrections.^b Indicates an upper limit.

3.4. The n-capture Elements

Out of the several neutron-capture elements that could be measured in our spectra, abundances of Sr and Ba could be derived for all of the program stars by the method of spectral synthesis. Both the lines at 4077 Å and 4215 Å were used to derive the Sr abundances, while the line at 4554 Å was used to derive the Ba abundance. The other strong Ba line at 4934 Å was avoided, as analysis of this line is extremely difficult, and

Table 12
Elemental Abundance Determinations for SDSS J1725+4202

Elements	Species	N_{lines}	$A(X)$	Solar	[X/H]	[X/Fe]	σ
Li	Li I	1	1.90				
C	CH	...	6.00	8.43	-2.43	0.07	synth
Na ^a	Na I	2	3.92	6.21	-2.29	0.21	synth
Mg	Mg I	4	5.53	7.59	-2.06	0.44	synth
Al ^a	Al I	1	3.37	6.43	-3.06	-0.56	synth
Ca	Ca I	8	4.28	6.32	-2.02	0.48	0.08
Sc	Sc II	5	0.63	3.15	-2.52	-0.02	0.09
Ti	Ti I	7	2.88	4.93	-2.05	0.45	0.08
	Ti II	6	2.87	4.93	-2.06	0.44	0.04
Cr	Cr I	3	3.03	5.62	-2.59	-0.09	0.07
	Cr II	2	3.46	5.62	-2.16	0.34	0.11
Mn	Mn I	4	2.60	5.42	-2.92	-0.32	0.15
Co	Co I	2	2.54	4.93	-2.39	0.11	0.09
Ni	Ni I	3	4.08	6.20	-2.12	0.38	synth
Zn	Zn I	2	2.71	4.56	-1.85	0.65	synth
Sr	Sr II	2	0.75	2.83	-2.08	0.42	synth
Ba	Ba II	2	0.00	2.25	-2.25	0.25	synth

Note.^a Values obtained after applying NLTE corrections.

yields large errors due to Fe blends found in the wings of this line (Gallagher et al. 2010). The average abundances for Sr and Ba for the present sample are $[\text{Sr}/\text{Fe}] = +0.26$ and $[\text{Ba}/\text{Fe}] = +0.25$. However, several additional n-capture elements could be detected in SDSS J065252.76+410506.0, which exhibits a large and uniform enhancement of n-capture elements. The first n-capture peak species—Sr, Y, and Zr—could be detected among the lighter n-capture elements, with an average value of $[\text{Is}/\text{Fe}] = +0.68$. Among the heavier n-capture elements, Ba, La, Nd, and Eu could be measured,

Table 13
Elemental Abundance Determinations for SDSS J1933+4524

Elements	Species	N_{lines}	$A(X)$	Solar	[X/H]	[X/Fe]	σ
Li	Li I	1	2.25				
C	CH	...	6.50	8.43	-1.93	-0.13	synth
Na ^a	Na I	2	4.23	6.21	-1.98	-0.18	synth
Mg	Mg I	4	5.95	7.59	-1.64	0.16	synth
Al ^d	Al I	1	3.85	6.43	-2.58	-0.78	synth
Ca	Ca I	8	4.86	6.32	-1.46	0.34	0.08
Sc	Sc II	5	1.62	3.15	-1.53	0.27	0.09
Ti	Ti I	7	3.60	4.93	-1.33	0.47	0.08
	Ti II	6	3.75	4.93	-1.18	0.62	0.04
Cr	Cr I	3	4.18	5.62	-1.44	0.36	0.07
	Cr II	2	4.15	5.62	-1.47	0.33	0.11
Mn	Mn I	4	3.59	5.42	-1.83	-0.03	0.15
Co	Co I	2	2.97	4.93	-1.96	-0.16	0.09
Ni	Ni I	3	4.52	6.20	-1.68	0.12	synth
Zn	Zn I	2	3.18	4.56	-1.38	0.42	synth
Sr	Sr I	2	1.60	2.83	-1.23	0.57	synth
Ba	Ba I	2	0.95	2.25	-1.30	0.50	synth
Eu ^b	Eu II	1	-0.50	0.52	-1.02	0.78	synth

Notes.

^a Values obtained after applying NLTE corrections.

^b Indicates an upper limit.

with an average value of $[\text{hs}/\text{Fe}] = +0.90$. The values of $[\text{hs}/\text{ls}] = +0.22$ and $[\text{Ba}/\text{Eu}] = -0.23$ indicate that SDSS J065252.76+410506.0 could have received contributions from both the r -process and s -process. However, the strong presence of Li, with $A(\text{Li}) = 1.75$, along with a low abundance of carbon ($[\text{C}/\text{Fe}] = -0.12$, corrected for evolutionary effects) rules out the possibility of s -process via mass transfer from a companion binary star or winds from a massive star (Susmitha et al. 2021). Hence, SDSS J065252.76+410506.0 is more likely to be of r -process origin. The possibility of i -process origin (Hampel et al. 2016; Denissenkov et al. 2017) needs to be further explored as well.

3.5. Kinematics

To obtain the stars' kinematics, we required distances, proper motions, and radial velocities. Fortunately, Gaia provides a unique opportunity to estimate the proper motions of the stars with high precision, which we have adopted from Gaia-EDR3 (Brown et al. 2021). Distances are obtained from the catalog of Bailer-Jones et al. (2021), who estimated the distances from Gaia-EDR3 parallaxes using probabilistic methods. The radial velocities were derived from the observed spectra, as listed in Table 1. We used the Astropy module to convert into the Galactocentric system and determined Galactocentric distances (X , Y , Z) and velocities (V_x , V_y , V_z), where the XY plane is the Galactic plane. For this conversion, we considered the Galactocentric distance for the Sun to be 8.2 kpc (Dehnen & Binney 1998; McMillan 2017), the distance of the Sun from the Galactic plane to be 0 kpc, and the solar velocity components to be (12.9, 245.6, 7.78) km s^{-1} (Meingast et al. 2021).

We also derived the orbital characteristics of the observed program stars (Matas Pinto et al. 2021). For our computation, we have used r to denote the Galactocentric distance. The parameter V_r is the velocity component along R , while V_z is the vertical component of the velocity of the stars. The parameter L_z represents the z component of angular momentum, and L_{\perp} denotes the perpendicular component of angular momentum.

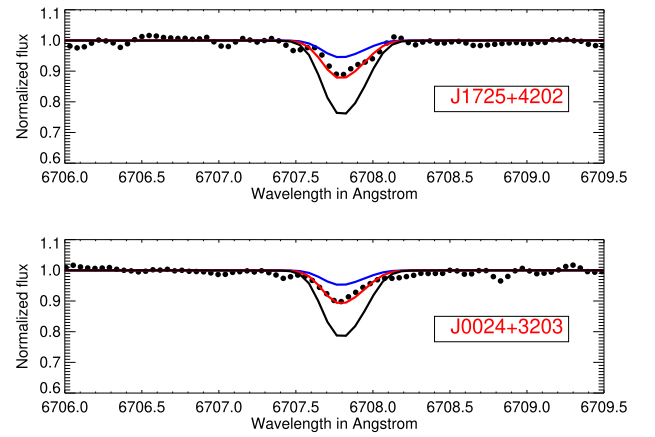


Figure 2. The synthesis of the Li line. The red line shows the best-fit synthetic spectrum, while black-filled circles indicate the observed spectra. The black and blue lines show the synthetic spectra for deviations in the Li abundance of 0.50 dex from the best fit.

The parameter V_{ϕ} corresponds to the azimuthal velocity and is given by L_z/R . All of the computed velocities and angular momenta for the program stars are listed in Table 3. The velocities are listed in km s^{-1} , whereas the angular momenta are listed in multiples of $10^2 \text{ kpc km s}^{-1}$. Following Di Matteo et al. (2020) and assuming a clockwise rotation of the disk, a negative value of V_{ϕ} represents prograde motion, whereas a positive value of V_{ϕ} represents retrograde motion. As shown in Figure 5, the dotted black line separates prograde motions from retrograde motions. Our program stars are evenly distributed in both regions; four stars toward the bottom left of the diagram likely belong to the disk population. SDSS J065252.76+410506.0, marked in red, also belongs to this group. The other stars on the Spite plateau from the literature are shown with green open circles. The blue semicircle shows the expected location of the disk stars in this plane.

4. Results and Discussion

4.1. Lithium Distribution in the Metal-poor Regime

We have demonstrated the distribution of Li abundances as a function of temperature for different stellar families in Figure 6. The stars have been further categorized into giants and dwarfs for the EMP, CEMP-no, and CEMP-s classes. The literature data are compiled from the SAGA database (Suda et al. 2008), and the program stars with detections of Li are marked as red diamonds. As noted by several studies on Li abundances in metal-poor stars (Spite & Spite 1982; Bonifacio et al. 2007; Spite et al. 2015), the plateau is observed for warmer dwarf stars with $T_{\text{eff}} > 5800 \text{ K}$. However, the scatter tends to increase as temperature decreases from 6500 to 5700 K. The identical distribution of Li across the EMP and CEMP-no stars indicates the interstellar medium to be well mixed during the epochs of their formation. Hence, Li could not be used as a yardstick to differentiate between these different stellar populations. However, Li is often depleted for CEMP-s stars but they are not considered for deriving the fits in Figure 6 as the Li in these stars is often accreted through mass transfer from a companion asymptotic giant branch (AGB) star. Mass transfer from a low-mass AGB star would produce large amounts of C and deplete Li, and also produce s -process-enhanced material. There are models in which AGB stars could produce Li through the

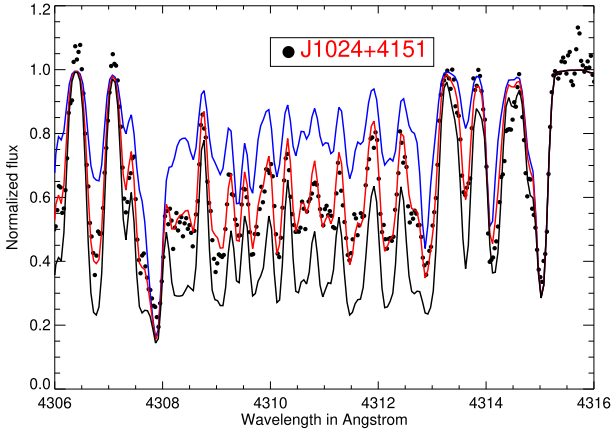


Figure 3. An example of spectral fitting for the molecular CH G-band region. The black-filled circles denote the observed spectra while the colored lines indicate the synthetic spectra. Red shows the best spectral fit, while black and blue lines indicate the spectra for C abundance deviating by ± 0.50 dex from the best fit.

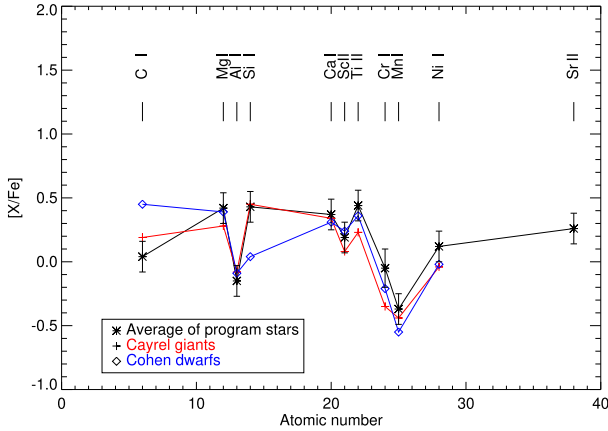


Figure 4. The nucleosynthesis pattern for the program stars, compared to the samples from Cayrel et al. (2004) and Cohen et al. (2004). The error bars corresponding to the uncertainties in the abundances for each element are shown as black lines.

Cameron–Fowler mechanism (Cameron & Fowler 1971). Through this mechanism, the outer convective envelope comes in contact with the H-burning shell where ${}^3\text{He}$ is being produced by proton–proton reactions. The ${}^3\text{He}$ is burned to ${}^7\text{Be}$ via ${}^3\text{He}(\alpha, \gamma){}^7\text{Be}$ under convective conditions. The ${}^7\text{Be}$ is then swept up to the stellar surface and decays to ${}^7\text{Li}$ by electron capture. Only three of our sample stars with measurable Li are MSTO stars, which is not adequate to test the consistency of the slope for our sample. Black and blue dots are used in Figure 6 for the literature sample to homogeneously differentiate between dwarfs (black) and giants (blue) for all classes of stars. The two outliers among the EMP stars shown as pink filled circles are CS22893-010 (Roederer et al. 2014) and C1012254-203007 (Ruchti et al. 2011).

We have demonstrated the trends for Li abundances in red giant branch (RGB) and MS stars (stars with $\log g$ values greater than 4 are considered to be MS stars) with temperature; definite trends are present. A strong correlation is obtained for RGB stars with a Pearson correlation coefficient of 0.89, while the dwarf MS stars exhibit a weaker correlation coefficient of 0.60. The probability of no correlation for the RGB and dwarf MS stars is less than 10^{-5} . The best fits for these two populations are shown as blue and black solid lines, respectively, in Figure 6. About 85% of the stars fall within

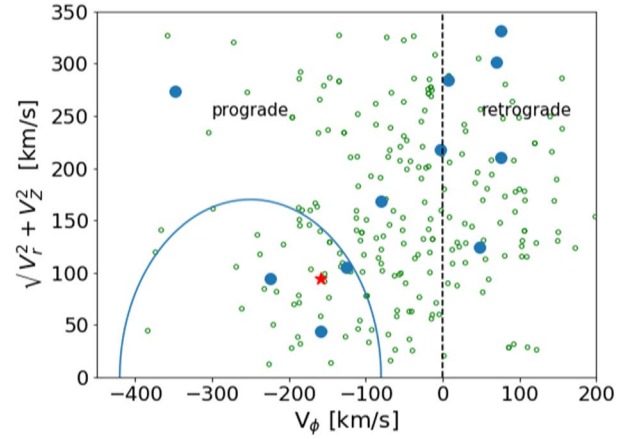


Figure 5. Toomre diagram exhibiting the orbital characteristics of the program stars. The dotted line indicates the split between prograde and retrograde motions. The blue-filled circles represent the program stars, while the red-filled star indicates SDSS J065252.76+410506.0. The blue semicircle shows the expected location of the disk stars in this diagram. The green open circles represent stars in the Spite plateau from the literature.

the 1σ width of the best fit shown by the solid lines in the plot. The errors for the Li abundances are taken to be 0.05 dex, while the error for temperature is taken to be 150 K. The empirical relations governing the best fit for the trends of $A(\text{Li})$ with T_{eff} in the giant stars and dwarf stars are given by relations (1) and (2), respectively:

$$A(\text{Li}) = 0.00108 T_{\text{eff}} - 4.524 \quad (1)$$

$$A(\text{Li}) = 0.00037 T_{\text{eff}} - 0.392. \quad (2)$$

Figure 7 shows the trend of Li abundance with metallicity. The cosmological value of Li and the observed value of the Spite plateau are shown by black lines. A small slope can be seen, and the scatter tends to increase for MS stars as metallicity decreases. The lowest-metallicity stars have lower values of $A(\text{Li})$, which reach the Spite plateau at $[\text{Fe}/\text{H}] > -3.50$, albeit with a large scatter. Our small sample could not yield significant results, but detection of Li in additional stars would provide better opportunities to understand the evolution and (possible) depletion of Li in the early universe.

4.2. Lithium Abundances in Halo and Globular Cluster Stars

Pasquini et al. (2005) found a trend for Li abundances with other elements, such as Na, O, and N, for the MSTO stars in NGC 6752. $A(\text{Li})$ was found to correlate with $[\text{O}/\text{Fe}]$ and anticorrelate with $[\text{Na}/\text{Fe}]$ and $[\text{N}/\text{Fe}]$. Bonifacio et al. (2007) confirmed the $A(\text{Li})$ – $[\text{Na}/\text{Fe}]$ anticorrelations in 47 Tucanae. However, no such trend was noticed among the halo stars. In Figure 8, the halo stars have been divided into dwarfs (black dots) and giants (blue dots). The depletion of $A(\text{Li})$ due to evolutionary mixing can be seen in all four panels. No trends could be seen for $A(\text{Li})$ with $[\text{Na}/\text{Fe}]$ (as reported in a few globular clusters), $[\text{Ca}/\text{Fe}]$ (representative of α -element abundances), $[\text{Cr}/\text{Fe}]$ (an Fe-peak element), and $[\text{Ba}/\text{Fe}]$ (an n-capture element). We have also marked the abundances of the globular cluster (GC) escapees (Bandyopadhyay et al. 2020b) and the CEMP-no star (Bandyopadhyay et al. 2018) with red-filled triangles and pink diamonds, respectively, in each of the panels.

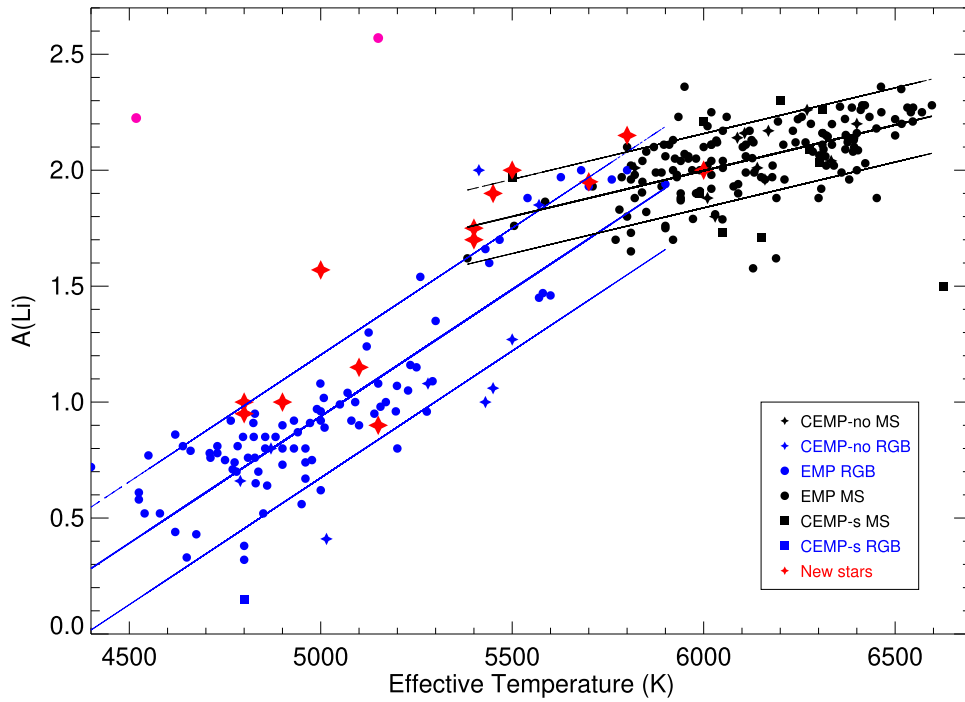


Figure 6. The distribution $A(\text{Li})$ as a function of T_{eff} for the different stellar families indicated in the figure. The program stars are marked by large red diamonds. The best fits for the giants (in blue) and dwarfs (in black) are shown by solid lines along with the 1σ regions for each fit. The slope and σ of the fit for the giants are $0.0012 \text{ dex K}^{-1}$ and 0.19 dex K^{-1} , respectively, while for the dwarfs they are $0.0005 \text{ dex K}^{-1}$ and 0.12 dex K^{-1} , respectively.

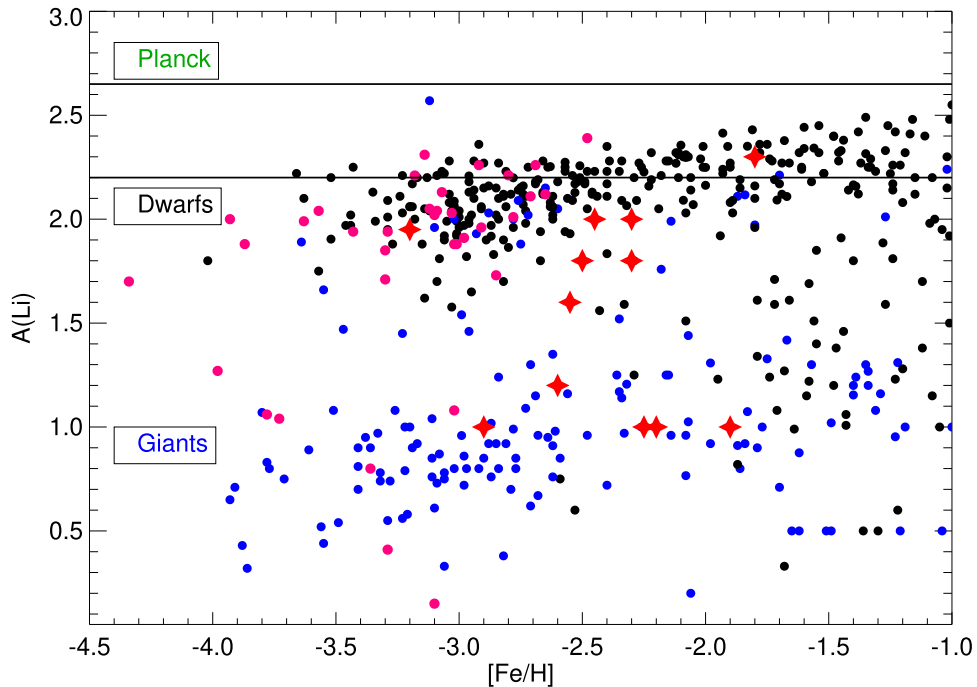


Figure 7. The distribution of $A(\text{Li})$ as a function of $[\text{Fe}/\text{H}]$. Predictions from the Planck mission and the Spite plateau abundances are shown by black solid lines. The dwarf stars are marked in black, while giant stars are marked in blue. CEMP-no stars are shown as red dots. The program stars with Li detections in this study are shown by filled red diamonds.

Lithium could also be detected for both of the GC escapees of this study, SDSS J064655.6+411620.5 and SDSS J193712.01+502455.5 (Bandyopadhyay et al. 2020b), and was found to be normal. Lithium is a fragile element, and is completely destroyed in a temperature range much lower than that required for the operation of the Mg–Al cycle. Thus, the presence of Li in second-generation stars

indicates a heavy dilution of the gas processed by p-capture reactions with unprocessed gas that still preserves the standard Population II lithium abundance (D’Antona et al. 2019). Lithium has been measured in several Galactic GCs (D’Orazi et al. 2015; D’Antona et al. 2019); their Li abundances exhibit a similar distribution to normal metal-poor halo stars.

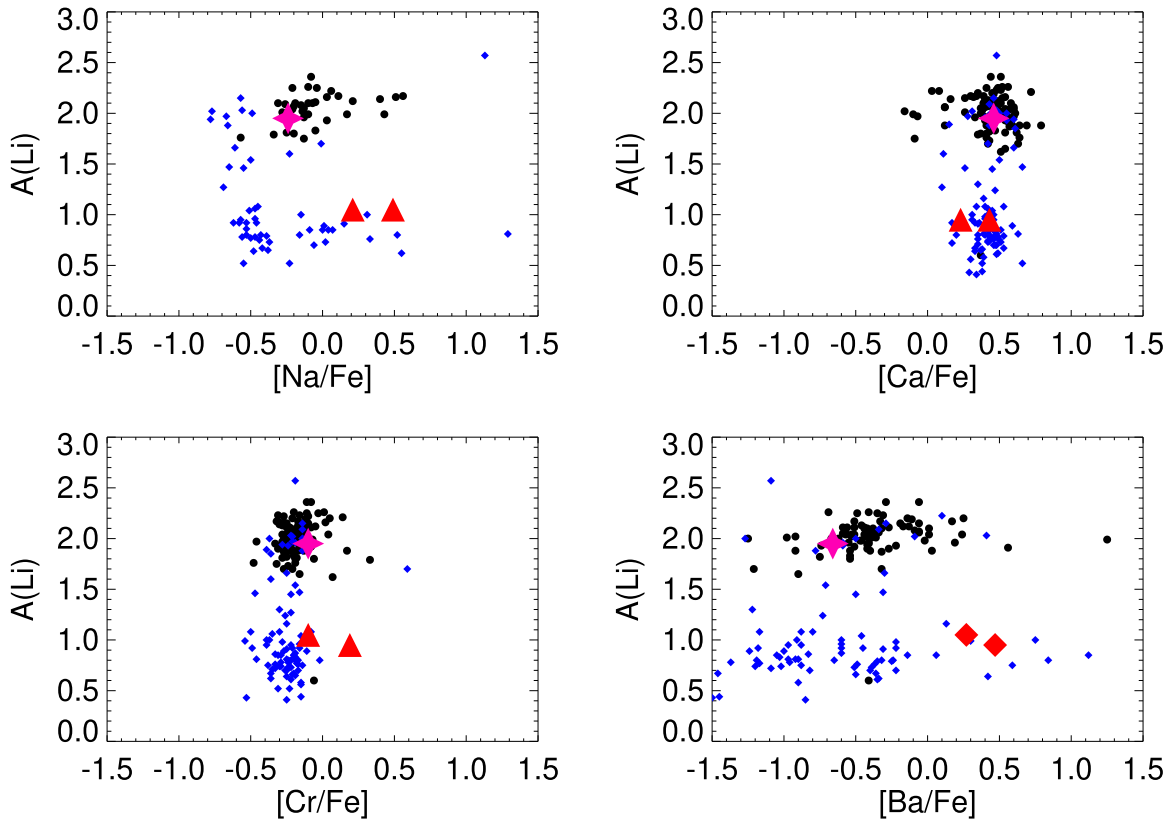


Figure 8. The Li abundance for VMP and EMP stars with detections of Li. The black dots mark the dwarf stars, while blue dots represent the giants. The GC escapees from this study are marked with red-filled triangles, and the CEMP-no star is marked with a pink diamond.

4.3. Li Abundance as a Function of Distance from the Galactic Plane

When combined with stars from the literature, we have 337 stars with Li, $[\text{Fe}/\text{H}]$, and RV information. In Figure 7, we showed that there is a plateau with a negative slope for the $A(\text{Li})$ distribution with $[\text{Fe}/\text{H}]$. We wanted to examine whether there is any correlation of the distribution of stars with respect to distance from the Galactic plane as a function of the $A(\text{Li})$ or $[\text{Fe}/\text{H}]$ abundances. As both the present sample and the stars from the literature are metal-poor and Population II stars, it is expected that they will be found more often in the halo.

Figure 9 shows the relationship between $A(\text{Li})$ and absolute distance from the Galactic plane, $|Z|$, color-coded to indicate $[\text{Fe}/\text{H}]$. The figure suggests that the Galactic disk ($|Z| < 2$ kpc) is mostly populated with relatively metal-rich stars, while a slight trend can be noticed between stars' distance from the Galactic plane and their Li abundance. The Li abundances in the stars tend to decrease as their distances from the Galactic plane increase. Most Li-rich stars are found to be in or close to the Galactic plane. The new sample of stars in this study is shown by filled diamonds with colors corresponding to their metallicity. They are found to populate the region within 2 kpc of the Galactic plane.

4.4. Light-element Abundances

The program stars exhibit the typical odd–even nucleosynthesis pattern exemplified by low Na, high Mg, and low Al (Truran & Arnett 1971; Umeda et al. 2000; Heger & Woosley 2002). The trends for the abundances of odd-Z and α -elements are shown in Figure 10. The giants and main-sequence stars exhibit a similar distribution for the light elements. They show the expected

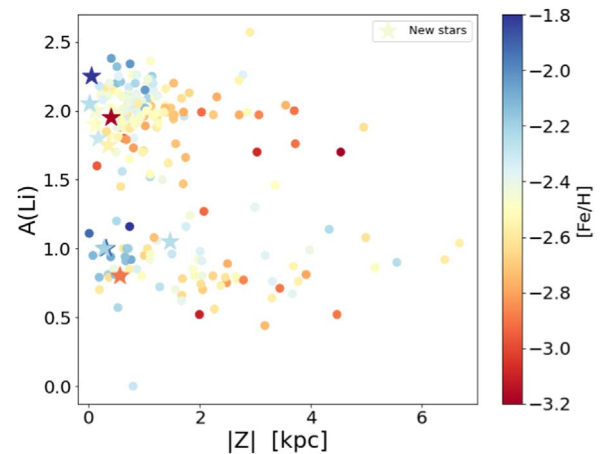


Figure 9. Li abundance as a function of distance from the Galactic plane. The color bar shows the metallicity of the stars. The new stars are marked by filled diamonds.

enhancement in α -elements for halo stars, with an average $[\alpha/\text{Fe}] = +0.41$. The α -elements Mg, Ca, and Ti exhibit a consistent overabundance, but a large scatter is observed in the case of Si. The star SDSS J065252.76+410506.0 (shown in red in Figure 10), apart from being rich in n-capture elements, also exhibits a higher abundance of the odd-Z element Na along with the α -elements. The light-element abundances for the program stars are found to agree with the previous investigations of metal-poor halo stars as shown in Figure 10. The data for the metal-poor halo stars were compiled from the SAGA database (Suda et al. 2008). The two GC escapees marked by filled blue diamonds

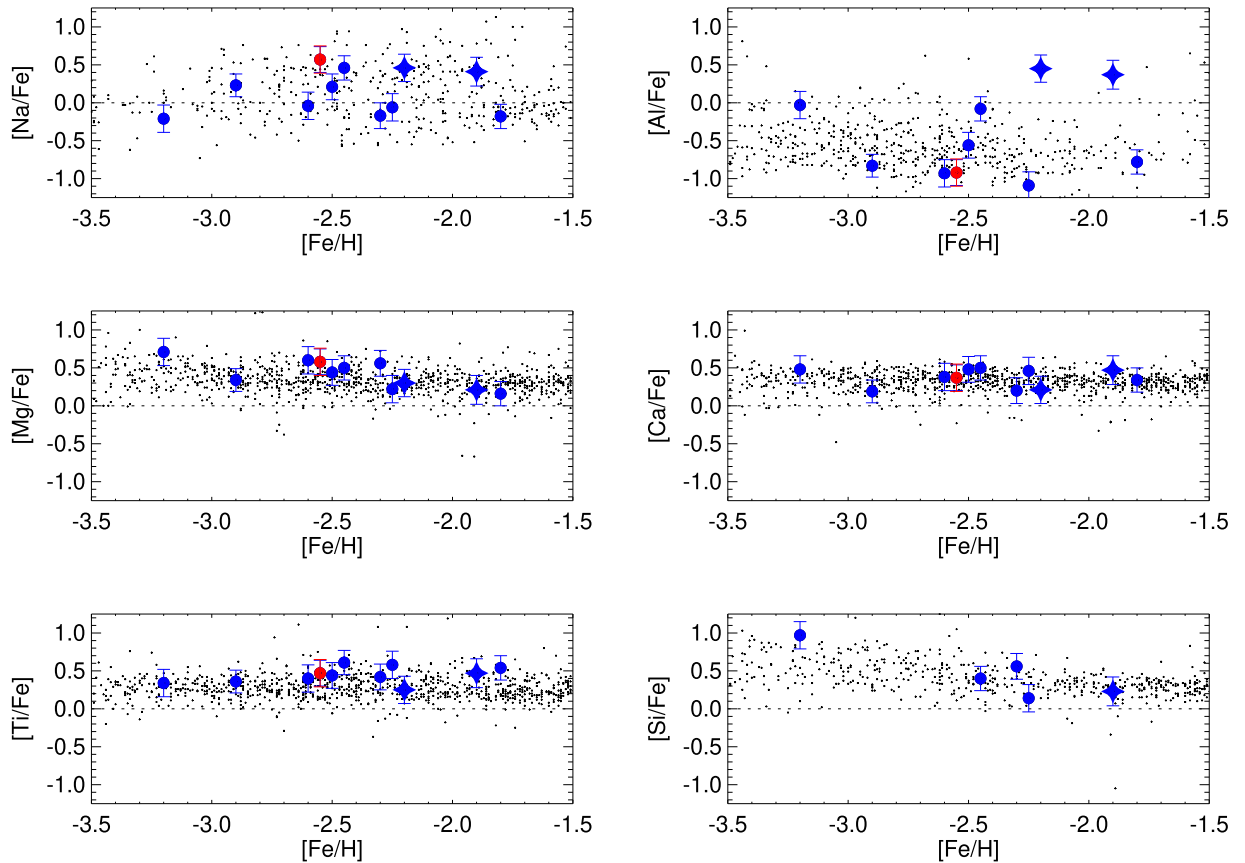


Figure 10. The distribution of the light elements Al, Mg, Ca, Ti, and Si as a function of $[\text{Fe}/\text{H}]$. The blue-filled circles represent the program stars, while the red-filled circle denotes the abundances for SDSS J065252.76+410506.0. The GC escapees are shown as blue-filled diamonds. The abundances of other metal-poor stars in literature compiled from Suda et al. (2008) are shown as black dots. The uncertainties are marked by colored error bars.

exhibit an elevated abundance of Al as seen in the top right panel. Si could be determined only for five out of the 11 stars as shown in the bottom panel.

4.5. Heavier-element Abundances

The heavier elements show the expected behavior with respect to variation in metallicity. The Fe-peak elements appear to closely track the Fe abundances (see Figure 11). Cobalt exhibits the typical decline with respect to increasing metallicity, the Ni and Zn abundances are slightly enhanced, and Mn is mostly depleted, as seen in other VMP stars. The decreasing trend in Cr with metallicity observed in metal-poor stars is due to the NLTE effects on neutral Cr, which varies with metallicity (Bergemann & Cescutti 2010). For our sample, Cr varies by 0.3 dex over a 1.4 dex range in metallicity. A large dispersion in Sc abundances was expected from chemical evolution models that include significant contributions from a few supernovae with different masses, but this is not found for the current sample. The well studied trend in abundances for the Fe-peak elements in metal-poor stars is demonstrated in Figure 11. The sample size for this study is not adequate to study the variation of individual elements with metallicity over a wide range but the program stars were found to follow the general trend. The large excess in Ni and Zn in a few stars could be attributed to a progenitor population of massive stars exploding as Type II supernovae (Nakamura et al. 1999; Nomoto et al. 2013). The uncertainties in the abundances of the program stars are also marked in Figure 11.

The distribution of the neutron-capture elements Sr and Ba is shown in Figure 12. Strontium belongs to the first-peak or lighter n-capture elements, while Ba belongs to the heavier n-capture elements. Large enhancement or depletion in n-capture elements is not found among our program stars, with the exception of SDSS J065252.76+410506.0. The ratio of light-to-heavy n-capture elements depends largely on the mass and nature of the progenitors. Since the contribution of the *s*-process is minimal at lower metallicities, the origin of these elements is expected to be the *r*-process. Following Tsujimoto & Shigeyama (2014a, 2014b), Susmitha Rani et al. (2016), and Siegel et al. (2019) for *r*-process origin, the heavier element Ba is produced primarily by neutron star mergers (NSMs) or collapsars, whereas the lighter element Sr can be synthesized in NSMs as well as Type II supernovae. Thus, an excess of one over the other indicates the dominance of either NSMs or core-collapse supernovae, and thus provides valuable information about the nature of the progenitors for the origin of the *r*-process (Bandyopadhyay et al. 2020a). For the present sample, the distribution of $[\text{Sr}/\text{Ba}]$, as a function of $[\text{Fe}/\text{H}]$, is shown in the bottom panel of Figure 12. From inspection, the scatter is very much lower, with a mean value of $\langle [\text{Sr}/\text{Ba}] \rangle = 0$, making them likely to be polluted evenly from both the progenitor population of NSMs and type II supernovae during their star formation epochs.

4.6. Kinematics

To study the assemblage history of the Milky Way, it is important to classify the origin of the stars based on their

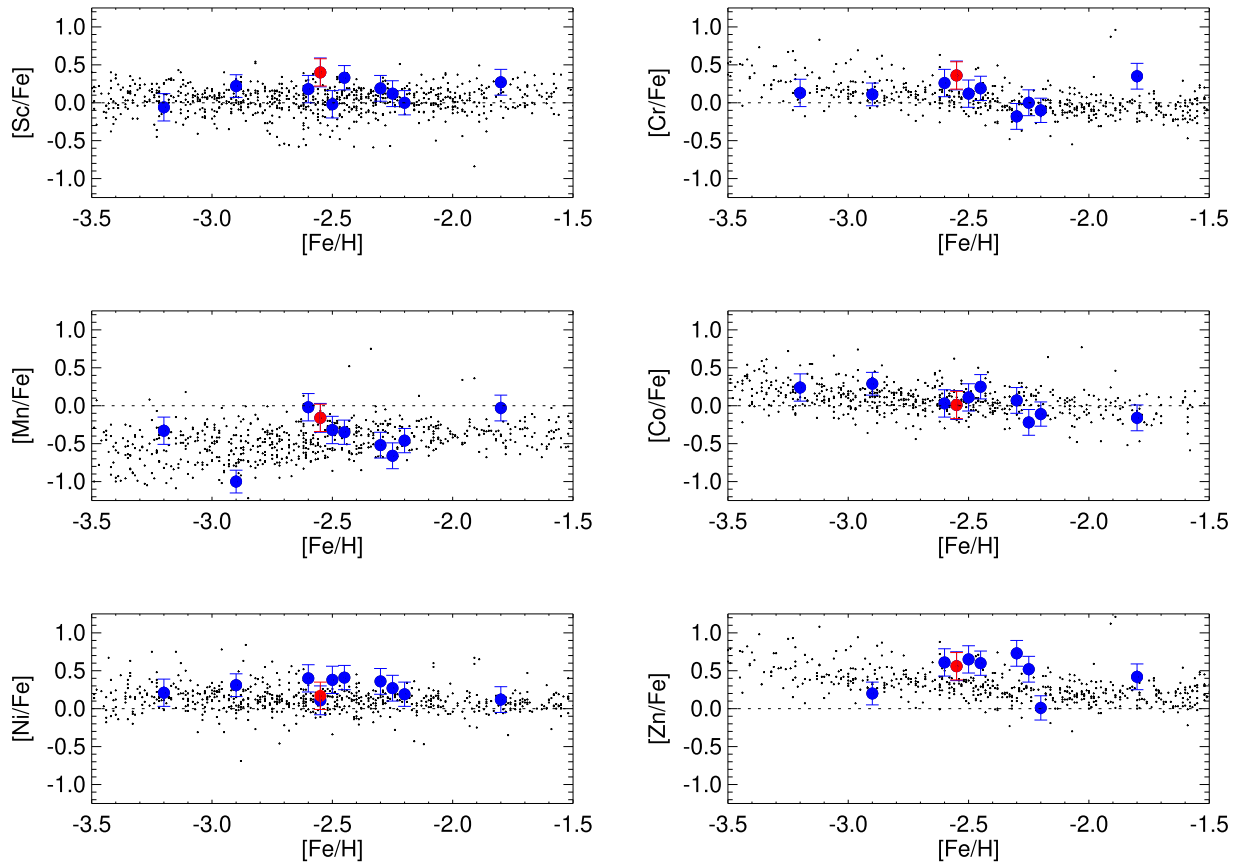


Figure 11. The distribution of the Fe-peak elements Sc, Cr, Mn, Co, Ni, and Zn as a function of $[\text{Fe}/\text{H}]$. The blue-filled circles represent the program stars, while the red-filled circle denotes the abundances for SDSS J065252.76+410506.0. The abundances of other metal-poor stars in literature compiled from Suda et al. (2008) are shown as black dots. The uncertainties are marked by colored error bars.

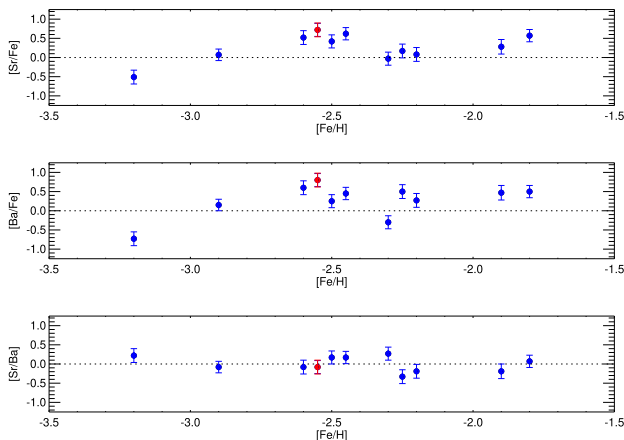


Figure 12. The distribution of the neutron-capture elements Sr and Ba as a function of $[\text{Fe}/\text{H}]$. The blue-filled circles represent the program stars, while the red-filled circle denotes the abundances for SDSS J065252.76+410506.0. The uncertainties are marked by colored error bars.

kinematics. The distribution of the Li-rich and Li-poor stars in the L_z versus L_\perp diagram can provide important clues to the evolution of Li in the Milky Way. Following Di Matteo et al. (2020), stars with $L_z < 10 \text{ kpc km s}^{-1}$ are mainly formed in situ while the stars in the region $L_\perp > 13 \text{ kpc km s}^{-1}$ and $L_z > 10 \text{ kpc km s}^{-1}$ are primarily accreted. However, the region $L_\perp < 13 \text{ kpc km s}^{-1}$ and $L_z > 10 \text{ kpc km s}^{-1}$ contains the stars from the Gaia–Sausage–Enceladus structure (Haywood et al. 2018; Helmi et al. 2018), as well as the disk stars with

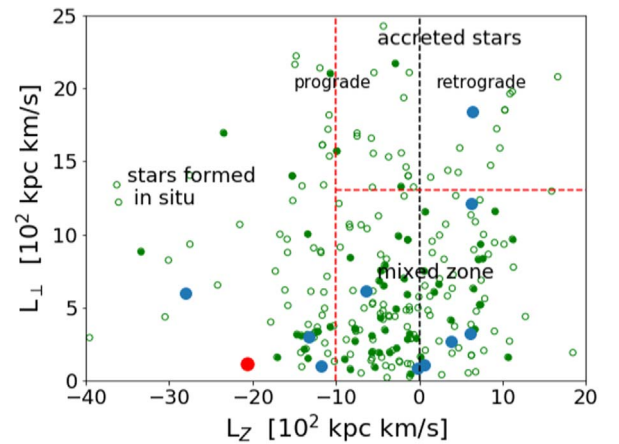


Figure 13. Orbital characteristics of the program stars. The black dotted line separates prograde motions from retrograde motions, while the red dotted lines show the regions dominated by stars formed in situ, accreted stars, and the mixed zone. The main-sequence and turnoff VMP and EMP stars with Li measurements compiled from Suda et al. (2008) are shown as green circles. The stars on the Spite plateau are shown as filled green circles, while slightly Li-poor stars are shown with green open circles.

kinematics similar to the halo, and is therefore called the “mixed zone.” The three regions are shown by red dashed lines in Figure 13, while the previously discussed classification of stars with prograde and retrograde motion is shown by the black dashed line. Four stars in the sample are found to have formed in situ, whereas one star is seen to be accreted. The rest

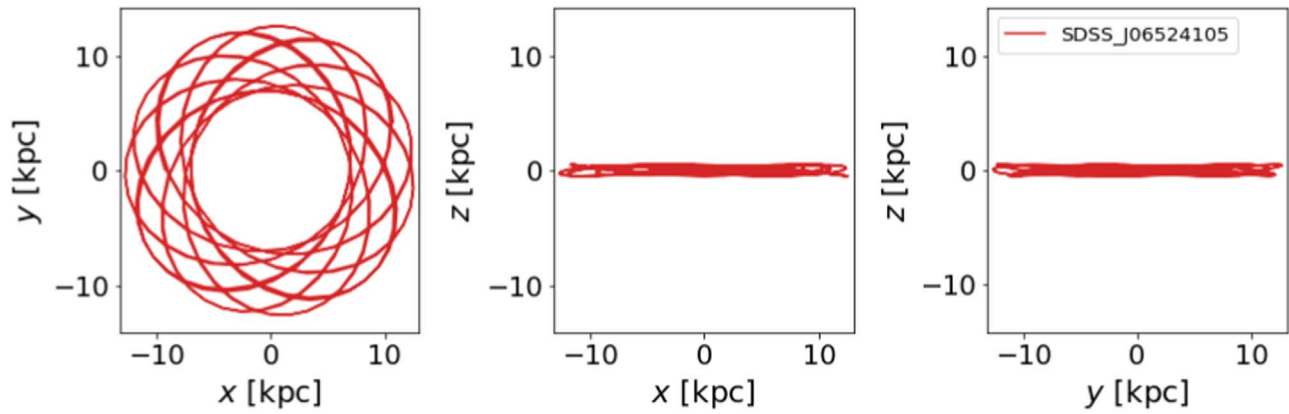


Figure 14. The trajectory of SDSS J0652+4105 in Galactocentric coordinates, which appears in the in situ region of Figure 13. The orbit is shown in the XY, XZ, and YZ planes. The trajectory has been calculated up to 5 Gyr back in time from the present day.

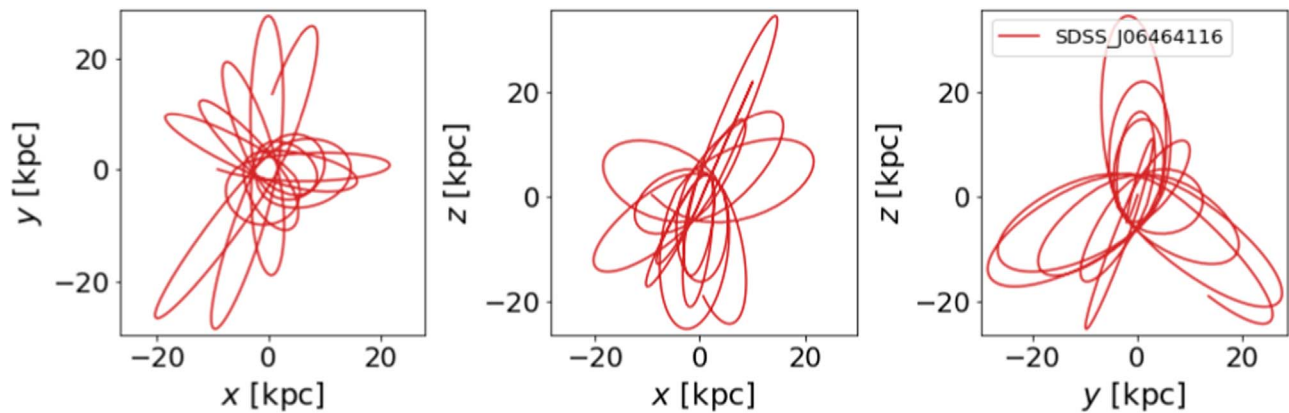


Figure 15. The same as Figure 14 for SDSS J0646+4116, which appears in the accreted region of Figure 13.

of the sample belongs to the mixed zone. The positions of the VMP and EMP stars in the Spite plateau from the SAGA database (Suda et al. 2008) are shown by green circles in Figure 13. The filled circles indicate the stars in the Spite plateau with $A(\text{Li}) > 2.05$, while the open green circles show the stars that are slightly depleted from the Spite plateau. The majority of the stars belong to the mixed zone, with very few populating either the in situ or accreted zones. The Li-rich stars are primarily found toward the bottom of the mixed zone. Thus, the Li population in the Spite plateau has significant contributions from both stars formed in situ and those that are accreted. However, only two of the Li-rich stars in the Spite plateau are found in the accreted zone, which is dominated by Li-depleted stars.

We have also calculated the trajectories for the stars in our sample for in situ, accreted, and mixed zones in the classification as shown in Figure 13. The orbits are computed using gala.⁹ The trajectories were calculated for a time period of 5 Gyr. The orbits for the in situ n-capture-rich star SDSS J065252.76+410506.0 are shown in Figure 14. The three

panels indicate the motions in the XY, XZ, and YZ planes. The star is found to have almost no motion along the Z-axis, and thus is clearly formed in situ as expected. Similarly, the orbit for the accreted star SDSS J064655.6+411620.5 is shown in Figure 15. However, the trajectory appears very similar to that of stars formed in situ, which could be possible, as SDSS J064655.6+411620.5 is also likely to be a globular cluster escapee. The mixed-zone program stars in this figure appear to have open orbits and hence are most likely to be accreted rather than formed in situ. The orbits for a few representative cases for the stars in the mixed zones are shown in Figure 16.

5. Conclusion

A sample of nine stars in the domain of very metal-poor stars with weak molecular carbon CH G -bands, selected from the low-resolution SDSS/MARVELS pre-survey, have been observed at a high spectral resolution to study their detailed abundances. The stars show typical α -element enhancements, and the odd-even nucleosynthesis pattern for the light elements. The Fe-peak elements mostly track the iron content; the observed trends are consistent with other metal-poor stars. Lithium could be detected and measured in all the program stars, and several belong to the Spite plateau. The depletion of Li is observed as the stars ascend the giant branch. The trends for depletion in Li with temperature are quantified; 85% of the stars were found to fall within the 1σ width (0.19 and 0.12 dex K^{-1} for giants and dwarfs, respectively) of the best fit.

⁹ The routine gala is an Astropy affiliated package for Galactic dynamics. gala provides functionality for representing analytic mass models that are commonly used in Galactic dynamics contexts for numerically integrating stellar orbits (e.g., Chapter 3 of Binney & Tremaine 2008). The gravitational potential models are defined by specifying parameters such as mass, scale radii, or shape parameters. Once defined, they can be used in combination with numerical integrators provided in gala to compute orbits. gala comes with a predefined, multicomponent, but simple model for the Milky Way that can be used for orbit integrations.

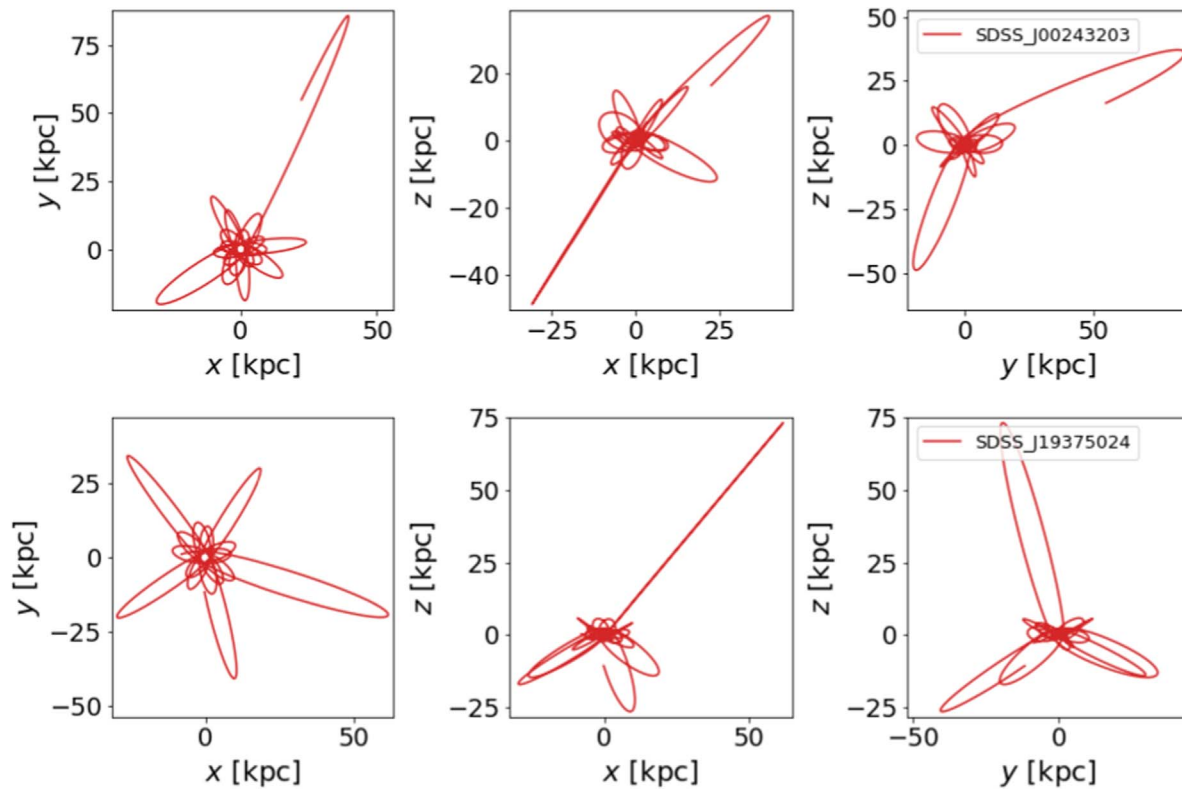


Figure 16. The same as Figure 14 for two representative stars falling in the mixed zone of Figure 13. The names of the individual stars are mentioned on the respective figures.

A small slope of the Spite plateau at the metal-poor end was also found when the Li abundance was studied as a function of Galactocentric distance, indicating that the Li-rich MSTO stars are not preferentially located at larger distances from the Galactic plane. Most Li-rich stars are found to be in or close to the Galactic plane. The stars have also been classified on the basis of their motion into prograde and retrograde samples. The program stars, along with the Spite plateau population in the literature, are divided into those that were likely formed in situ, accreted, and in the mixed zone. The orbits for the program stars have also been derived and studied for a period of 5 Gyr backwards in time. The mixed zone is found to be the most populated, and thus neither formation in situ nor by accretion can be considered as an important contributor to the population of the Spite plateau.

We thank the staff of IAO, Hanle, and CREST, Hosakote, who made these observations possible. The facilities at IAO and CREST are operated by the Indian Institute of Astrophysics, Bangalore. T.C.B. acknowledges partial support from grant PHY 14-30152 (Physics Frontier Center/JINA-CEE), awarded by the U.S. National Science Foundation (NSF). We also thank the anonymous referee for comments that improved the quality of our paper.

ORCID iDs

Avrajit Bandyopadhyay <https://orcid.org/0000-0002-8304-5444>

Thirupathi Sivarani <https://orcid.org/0000-0003-0891-8994>

Timothy C. Beers <https://orcid.org/0000-0003-4573-6233>

Prasanta K. Nayak <https://orcid.org/0000-0002-4638-1035>

Jeewan C. Pandey <https://orcid.org/0000-0002-4331-1867>

References

- Alvarez, R., & Plez, B. 1998, *A&A*, **330**, 1109
- Andrievsky, S. M., Spite, M., Korotin, S. A., et al. 2007, *A&A*, **464**, 1081
- Andrievsky, S. M., Spite, M., Korotin, S. A., et al. 2008, *A&A*, **481**, 481
- Aoki, W., Barklem, P. S., Beers, T. C., et al. 2009, *ApJ*, **698**, 1803
- Bailer-Jones, C. A. L., Rybizki, J., Fousneau, M., Demleitner, M., & Andrae, R. 2021, *AJ*, **161**, 147
- Bandyopadhyay, A., Sivarani, T., & Beers, T. C. 2020a, *ApJ*, **899**, 22
- Bandyopadhyay, A., Sivarani, T., Susmitha, A., et al. 2018, *ApJ*, **859**, 114
- Bandyopadhyay, A., Thirupathi, S., Beers, T. C., & Susmitha, A. 2020b, *MNRAS*, **494**, 36
- Bayo, A., Rodrigo, C., Barrado Y Navascués, D., et al. 2008, *A&A*, **492**, 277
- Beers, T. C., & Christlieb, N. 2005, *ARA&A*, **43**, 531
- Bergemann, M., & Cescutti, G. 2010, *A&A*, **522**, A9
- Bergemann, M., Gallagher, Andrew, J., Eitner, P., et al. 2019, *A&A*, **631**, A80
- Bergemann, M., & Gehren, T. 2008, *A&A*, **492**, 823
- Binney, J., & Tremaine, S. 2008, *Galactic Dynamics: Second Edition* (Princeton, NJ: Princeton Univ. Press)
- Bonifacio, P., Caffau, E., Spite, M., et al. 2015, *A&A*, **579**, A28
- Bonifacio, P., Molaro, P., Sivarani, T., et al. 2007, *A&A*, **462**, 851
- Bonifacio, P., Spite, M., Cayrel, R., et al. 2009, *A&A*, **501**, 519
- Brown, A. G. A., Vallenari, A., Prusti, T., et al. 2021, *A&A*, **650**, C3
- Cameron, A. G. W., & Fowler, W. A. 1971, *ApJ*, **164**, 111
- Castelli, F., & Kurucz, R. L. 2004, in *Modelling of Stellar Atmospheres*, Poster Contributions. Proc. of the 210th Symp. of the IAU (San Francisco, CA: ASP)
- Cayrel de Strobel, G., & Spite, M. 1988, in *IAU Symp. 132, The Impact of Very High S/N Spectroscopy on Stellar Physics* (Dordrecht: Springer)
- Cayrel, R., Depagne, E., Spite, M., et al. 2004, *A&A*, **416**, 1117
- Coc, A., Vangioni-Flam, E., Descouvemont, P., Adahchour, A., & Angulo, C. 2004, *ApJ*, **600**, 544
- Cohen, J. G., Christlieb, N., McWilliam, A., et al. 2004, *ApJ*, **612**, 1107
- D'Antona, F., Ventura, P., Marino, A. F., et al. 2019, *ApJ*, **871**, L19
- Dehnen, W., & Binney, J. 1998, *MNRAS*, **294**, 429
- Denissenkov, P. A., Herwig, F., Battino, U., et al. 2017, *ApJ*, **834**, L10
- Di Matteo, P., Spite, M., Haywood, M., et al. 2020, *A&A*, **636**, A115
- D'Orazi, V., Gratton, R. G., Angelou, G. C., et al. 2015, *MNRAS*, **449**, 4038
- Eisenstein, D. J., Weinberg, D. H., Agol, E., et al. 2011, *AJ*, **142**, 72

- Frebel, A. 2018, [ARNPS](#), **68**, 237
- Frebel, A., & Norris, J. E. 2015, [ARA&A](#), **53**, 631
- Gallagher, A. J., Ryan, S. G., García Pérez, A. E., & Aoki, W. 2010, [A&A](#), **523**, A24
- Ge, J., Thomas, N. B., Li, R., et al. 2015, AAS Meeting, **225**, 409.03
- Hempel, M., Stancliffe, R. J., Lugaro, M., & Meyer, B. S. 2016, [ApJ](#), **831**, 171
- Haywood, M., Di Matteo, P., Lehnert, M. D., et al. 2018, [ApJ](#), **863**, 113
- Heger, A., & Woosley, S. E. 2002, [ApJ](#), **567**, 532
- Helmi, A., Babusiaux, C., Koppelman, H. H., et al. 2018, [Natur](#), **563**, 85
- Korn, A. J., Grundahl, F., Richard, O., et al. 2006, [Natur](#), **442**, 657
- Lai, D. K., Bolte, M., Johnson, J. A., et al. 2008, [ApJ](#), **681**, 1524
- Matas Pinto, A. M., Spite, M., Caffau, E., et al. 2021, [A&A](#), **654**, A170
- McMillan, P. J. 2017, [MNRAS](#), **465**, 76
- McWilliam, A. 1998, [AJ](#), **115**, 1640
- Meingast, A., João, & Alena, R. 2021, [A&A](#), **645**, A84
- Nakamura, T., Umeda, H., Nomoto, K., Thielemann, F.-K., & Burrows, A. 1999, [ApJ](#), **517**, 193
- Nomoto, K., Kobayashi, C., & Tominaga, N. 2013, [ARA&A](#), **51**, 457
- Pasquini, L., Bonifacio, P., Molaro, P., et al. 2005, [A&A](#), **441**, 549
- Piau, L., Beers, T. C., Balsara, D. S., et al. 2006, [ApJ](#), **653**, 300
- Pinsonneault, M. H., Walker, T. P., Steigman, G., & Narayanan, V. K. 1999, [ApJ](#), **527**, 180
- Placco, V. M., Frebel, A., Beers, T. C., et al. 2014, [ApJ](#), **781**, 40
- Roederer, I. U., Preston, G. W., Thompson, I. B., Shtetman, S. A., & Sneden, C. 2014, [ApJ](#), **784**, 158
- Ruchti, G. R., Fulbright, J. P., Wyse, R. F. G., et al. 2011, [ApJ](#), **743**, 107
- Ryan, S. G., Gregory, S. G., Kolb, U., Beers, T. C., & Kajino, T. 2002, [ApJ](#), **571**, 501
- Ryan, S. G., Norris, J. E., & Beers, T. C. 1999, [ApJ](#), **523**, 654
- Sbordone, L., Bonifacio, P., Caffau, E., et al. 2010, [A&A](#), **522**, A26
- Siegel, D. M., Barnes, J., & Metzger, B. D. 2019, [Natur](#), **569**, 241
- Spergel, D. N., Verde, L., Peiris, H. V., et al. 2003, [ApJS](#), **148**, 175
- Spite, F., & Spite, M. 1982, [A&A](#), **115**, 357
- Spite, M., Cayrel, R., Plez, B., et al. 2005, [A&A](#), **430**, 655
- Spite, M., Spite, F., Caffau, E., & Bonifacio, P. 2015, [A&A](#), **582**, A74
- Sriram, S., Kumar, A., Surya, A., et al. 2018, [Proc. SPIE](#), **10702**, 2007
- Suda, T., Katsuta, Y., Yamada, S., et al. 2008, [PASJ](#), **60**, 1159
- Susmitha, A., Ojha, D. K., Sivarani, T., et al. 2021, [MNRAS](#), **506**, 1962
- Susmitha Rani, A., Sivarani, T., Beers, T. C., et al. 2016, [MNRAS](#), **458**, 2648
- Truran, J. W., & Arnett, W. D. 1971, [Ap&SS](#), **11**, 430
- Tsujimoto, T., & Shige-yama, T. 2014a, [ApJL](#), **795**, L18
- Tsujimoto, T., & Shige-yama, T. 2014b, [A&A](#), **565**, L5
- Umeda, H., Nomoto, K., Nakamura, T., et al. 2000, in *The First Stars*, ed. A. Weiss, T. G. Abel, & V. Hill (Berlin: Springer), 150